Journal of Physics D: Applied Physics

**PAPER**

# External magnetic field guiding in HiPIMS to control $sp^3$ fraction of tetrahedral amorphous carbon films

To cite this article: Behnam Akhavan *et al* 2021 *J. Phys. D: Appl. Phys.* **54** 045002

View the article online for updates and enhancements.

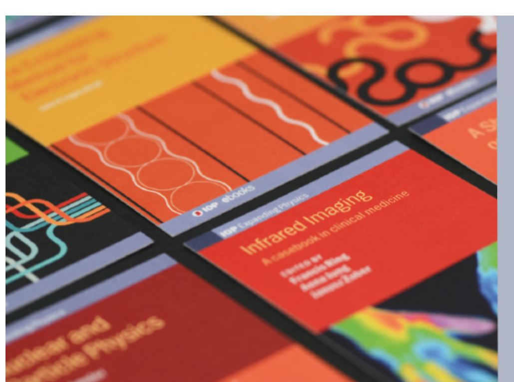

IOP ebooks™

Bringing together innovative digital publishing with leading authors from the global scientific community.

Start exploring the collection–download the first chapter of every title for free.

This content was downloaded from IP address 130.89.46.78 on 05/11/2020 at 13:51

J. Phys. D: Appl. Phys. 54 (2021) 045002 (12pp) https://doi.org/10.1088/1361-6463/abb9d2

# External magnetic field guiding in HiPIMS to control $sp^3$ fraction of tetrahedral amorphous carbon films

**Behnam Akhavan[1,2,3], Rajesh Ganesan[2,4], Stephen Bathgate[2], Dougal G McCulloch[5], James G Partridge[5], Mihail Ionsecu[6], Dave T A Mathews[7], Michael Stueber[8], Sven Ulrich[8], David R McKenzie[2,3,9] and Marcela MM Bilek[1,2,3,9]**

[1] School of Biomedical Engineering, University of Sydney, Sydney, NSW 2006, Australia
[2] School of Physics, University of Sydney, Sydney, New South Wales 2006, Australia
[3] Sydney Nano Institute, University of Sydney, Sydney, New South Wales 2006, Australia
[4] IHI Hauzer Techno Coating B.V., 5928 LL, Venlo, The Netherlands
[5] School of Science, RMIT University, GPO Box 2476 V, Melbourne, Victoria 3001, Australia
[6] Australian Nuclear Science and Technology Organisation, New Illawarra Rd, Sydney, NSW 2234, Australia
[7] Faculty of Engineering Technology, University of Twente, Enschede 7522LW, The Netherlands
[8] Institute for Applied Materials (IAM), Karlsruhe Institute of Technology (KIT), 76344, Eggenstein-Leopoldshafen, Germany
[9] Charles Perkins Centre, University of Sydney, Sydney, New South Wales 2006, Australia

E-mail: behnam.akhavan@sydney.edu.au and marcela.bilek@sydney.edu.au

Received 5 August 2020, revised 1 September 2020
Accepted for publication 18 September 2020
Published 4 November 2020

**Abstract**

Amorphous carbon films have many applications that require control over their $sp^3$ fraction to customise the electrical, optical and mechanical properties. Examples of these applications include coatings for machine parts, biomedical and microelectromechanical devices. In this work, we demonstrate the use of a magnetic field with a high-power impulse magnetron sputtering (HiPIMS) source as a simple, new approach to give control over the $sp^3$ fraction. We provide evidence that this strategy enhances the deposition rate by focusing the flux, giving films with high tetrahedral bonding at the centre of the deposition field and lower $sp^3$ fractions further from the centre. Resistive switching appears in films with intermediate $sp^3$ fractions. The production of thin amorphous carbon films with selected properties without the need for electrical bias opens up applications where insulating substrates are required. For example, deposition of $sp^3$ rich films on polymers for wear resistant coatings as well as fabrication of resistive switching devices for neuromorphic technologies that require tuning of the $sp^3$ fraction on insulating substrates are now possible.

Keywords: HiPIMS, magnetron sputtering, carbon film, tetrahedral amorphous-carbon, resistive switching

(Some figures may appear in colour only in the online journal)

 © 2020 IOP Publishing Ltd Printed in the UK

## 1. Introduction

Tetrahedral amorphous-carbon (ta-C) coatings contain a majority of tetrahedrally coordinated carbon atoms. ta-C coatings exhibit excellent resistance to corrosion, wear, and biofouling [1–5] and have chemical inertness and biocompatibility [6, 7]. These coatings have become increasingly popular for a wide variety of industrial and commercial applications including machine parts [8, 9], bearings [10], microelectromechanical devices, biomedical instruments and sensors [6, 11–13].

The $sp^3$ fraction in ta-C is determined by the impinging energy of depositing carbon ions. Maximizing the fraction of $sp^3$ bonds in ta-C is important for enhancing the coating's properties such as indentation hardness, optical gap, transparency and carrier properties for semiconductor devices [2, 3]. In order to generate the highest fraction of $sp^3$ bonds in a film formed by growth from carbon ions and neutral atoms, energies in the region of 100 eV are required [2]. Films with $sp^3$ fractions of up to about 85% have been deposited using processes such as filtered cathodic arc deposition (FCVA) [2, 14, 15], laser ablation [16], and mass-selected ion beam deposition [17, 18].

These methods, however, each have limitations such as the presence of macro-particles [19], coating non-uniformity on large areas [20] and limited deposition rate. Several attempts have been made to deposit ta-C films by conventional magnetron sputtering, since this process is scalable for low cost production. However, controlling the kinetic energy of the sputtered carbon atoms is not possible, as most of them are neutral. Electrostatic bias of the growing film increases the energy and flux of the background gas ions and causes them to be implanted into the film, increasing their concentration in the film without optimizing the carbon $sp^3$ fraction. Recently, we have demonstrated a process, known as mixed mode HiPIMS, for depositing ta-C from a graphite target that has advantages of reduced macroparticle content and compatibility with large area, high-rate coating systems [21–23].

In all methods of ta-C coating by sputtering reported so far [21, 24–26], it is necessary to apply a negative bias voltage to the substrate in order to increase the impact energy of carbon ions to place it within an optimum range around 100 eV. In previous works [21, 23], energies of carbon ions were increased by applying negative bias to the substrate. However, for deposition onto large area substrates or onto insulating substrates, it is advantageous to deposit ta-C without the need for substrate bias. For example, to deposit ta-C coatings onto non-conducting, large area or moving substrates as in architectural and other high-volume production applications, it is impractical or even impossible to apply voltages in the range of 100 V. Therefore, it would be of great interest to develop a HiPIMS deposition source that provides the optimum energy in the absence of substrate bias. This would make possible the deposition of ta-C coatings on a wide variety of substrates across a range of processes.

Here we demonstrate that the optimum energy of carbon ions for ta-C formation with the highest $sp^3$ content can be obtained without the application of substrate bias by placing a simple current-carrying coil between the target and the substrate holder. We provide evidence that integrating such a magnetic field configuration to a mixed mode HiPIMS sputtering process is a successful approach to produce ta-C films with controlled $sp^3$ fraction.

## 2. Materials and methods

The deposition of carbon films was performed using an AJA 1800-F sputtering system equipped with a vacuum chamber with a diameter of 67.6 cm and a height of 50.8 cm. Further details of the sputtering system have been reported earlier [22, 27, 28]. The chamber was evacuated to the base pressure of at least $4.7 \times 10^{-5}$ Pa using a rotary-backed turbomolecular pump (Shimadzu 1003 LM). The depositions were carried out at a working pressure of 0.225 Pa using argon gas. A RUP7 pulsed power supply (GBS-Electronik GmbH, Germany) was utilized to power the magnetron. This power supply could deliver a peak voltage of 1000 V and a peak current of 400 A. The power supply is voltage regulated so that the discharge current is determined by the plasma impedance. Voltage pulses of 640 V were applied with a pulse length of 200 $\mu$s at a frequency of 100 Hz. The sputtering system is schematically shown in figure 1.

A 6 mm thick compressed graphite target (Plansee, Germany) with a diameter of 76.7 mm was used for all deposition experiments. The target was mounted with a copper mesh underneath to allow for good thermal contact with the machined surface of the water-cooled magnetron target holder. The deposition time of 30 min was kept constant for all samples.

The external magnetic field was generated above the target using a coil positioned on electrically floating brackets on top of the magnetron source, as shown schematically in figure 2(a). The coil was made by winding 20 turns of copper tube around a Teflon cylinder of dimensions described elsewhere [29, 30]. The inner and outer diameters of the coil were 87.0 and 93.4 mm, respectively. The distance between the coil to the magnetron surface was 17 mm from the first turn. The distance between the last turn of the coil and the substrate was 70 mm. The coil was capable of generating magnetic fields of up to 10 mT within 1 $\mu$s when 120 A of current was passed through the coil at a voltage of 800 V. The magnetic field density was measured on the racetrack, where the magnetic field perpendicular to the target surface ($B\perp$) is minimum. Care was taken to apply the external magnetic field in a direction that reinforced the magnetron field's outer field lines to achieve greater target current, higher fluence of ions arriving at the substrate, and greater deposition rate. The other direction of applied magnetic field prevented the stability of magnetron operation for magnetic coil currents of greater than 90 A. The time-resolved pattern of the current in the coil together with the HiPIMS voltage pulse are presented in figure 2(b). Current-time traces recorded for discharges with and without the coil current are shown in figure 2(c).

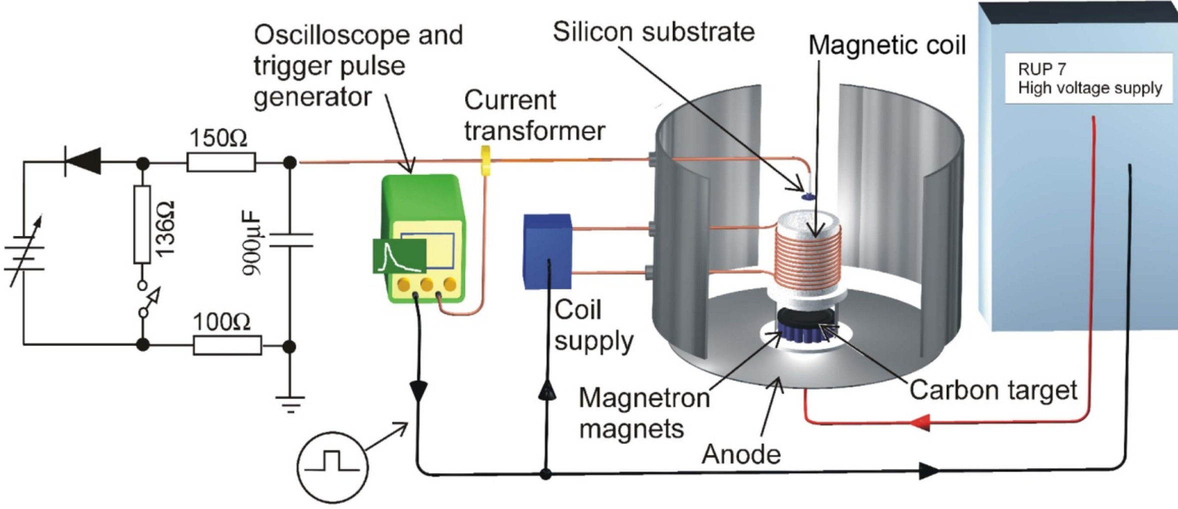


**Figure 1.** Schematic illustration of the HiPIMS sputtering system used to fabricate ta-C films. A magnetic coil, powered by a separate pulsed power supply, was placed between the target and the substrate. The coil current was triggered with a time delay with respect to the onset of the HiPIMS voltage pulse. Arrows indicate the signal input pathways.

The external magnetic field was applied during the short-lived arc portion of the discharge, that is, in the 'mixed mode', during which a higher ionization of sputtered carbon atoms occurs, enabling more efficient transport of the carbon to the substrate. This was achieved by setting a delay of 150 $\mu$s between the onset of the HiPIMS voltage pulse and the application of current (180 A) to the coil [29, 30]. The 150 $\mu$s delay was found to be the optimum delay, as previously observed for a hafnium target with the same magnetic field coil [29]. The coil voltage was turned off when the HiPIMS pulse terminated. A pulse generating function in the 200 MHz oscilloscope (DSO-X 2014 A) was used as a central hub to synchronously trigger the HiPIMS voltage source (RUP7) and the coil power supply.

The substrates were placed on the substrate holder at various positions with respect to the axis of the coil and therefore the centre of target, as schematically represented in figure 2(a). A negative bias voltage of—25 V was applied to the substrate to repel electrons and attract ions to the substrate for ion current measurements. A bias voltage of −25 V was also applied to the substrates during the HiPIMS deposition. This voltage, that is normally too low to achieve sp3 bonding, is similar to the floating potential on insulating substates. A 900 $\mu$F capacitor maintained the bias voltage constant in the presence of the large current during the discharge pulses. Variations in substrate current at different locations of the substrate holder with varying coil currents were used to determine the localized deposition flux.

The ion energy was measured using a retarding field energy analyzer (RFEA) of the same type that has been used for measurements of the energy of copper ions in HiPIMS [31] and the energy of copper ions in a copper cathodic vacuum arc [32, 33]. The aperture of the RFEA had a diameter of 24 mm, and the analyzer had an enclosed volume and a grid at the entrance to extract the ions from the plasma that were then detected by a single plate collector. The current of ions was measured as a function of the retarding voltage between the grid and the collector plate and the energy distribution was calculated by differentiating the curve of ion current as a function of the voltage difference between the grid and the plate.

To provide an indication of the composition of plasma ions reaching the substrate and their energy spectrum in the absence of the magnetic coil, we used a Hiden mass spectrometer (Hiden EQP System high transmission ion energy analyser and quadrupole mass spectrometer) and an impedance energy analyser respectively, in the same model AJA magnetron sputtering system using the same graphite target and the same sputtering conditions, pressure and gas type.

Metal-insulator-semiconductor (MIS) structures were formed from the carbon films deposited on silicon <100> wafers by sputtering platinum contacts of diameter 0.35 mm. The substrates were boron doped, *P*-type with resistance between 1–4 Ohm.cm and thickness of 680 micrometres. The current-voltage (I–V) characteristics of these devices were measured using a semiconductor parameter analyser (HP4155A).

The thickness, refractive index ($n$), and extinction coefficient ($k$) of the deposited carbon films were determined using a spectroscopic ellipsometer (2000D, JA Woollam Co.). The accuracy of thickness values measured using the ellipsometer was confirmed by results obtained using a KLA Tencor stylus profilometer. The $n$ and $k$ values as a function of wavelength were calculated in the wavelength range of 192.5–1000 nm from spectroscopic ellipsometry data using a Cauchy optical model for the film and substrate in the configuration of ta-C/$SiO_2$/c-Si (100). The optical constants of the crystalline Si $< 100 >$ and passive silicon dioxide ($SiO_2$) layer [34] were set as fixed variables. To achieve a suitable fit, thicknesses within 1.6 to 1.8 nm were required for the $SiO_2$ layer.

High resolution transmission electron microscopy (CM200 Philips Supertwin TEM) was used to obtain the electron energy loss spectrum for the samples in the low loss and K

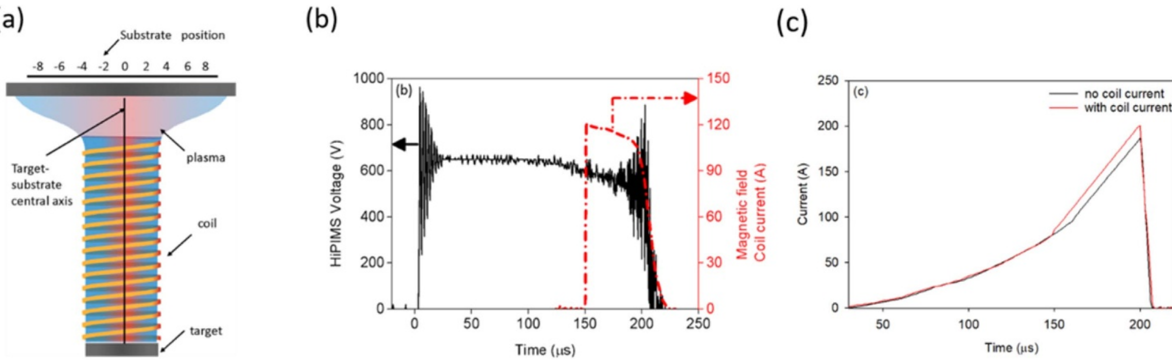


**Figure 2.** (a) Schematic diagram of the target, coil and position of the substrates placed in the deposition system (left). The target-substrate central axis is denoted by the black line drawn perpendicular to the position '0′ indicating the intersection of the substrate and the central axis of the target. The substrates were located at all positions from + 8 to − 8 cm. (b) The time-resolved pattern of the current pulse in the coil generating the external magnetic field (red; right axis) is presented together with the HiPIMS voltage pulse (black; left axis). (c) Current-time traces for discharges with and without the coil current.

near edge regions with an energy resolution of 0.2 eV. The $sp^2$ fraction was obtained using the EELS carbon K edge. A glassy carbon sample was used as a reference for 100% $sp^2$ bonding. The corresponding $sp^3$ fraction was determined by the method described in Berger *et al* [35]. In this method, the area of the 1 s to $\pi^*$ feature at 284 eV is calculated under the assumption that no sp bonds are present in the film. The deposited films are unlikely to have sp bonds, as their hydrogen content was almost negligible (<0.2%). This was confirmed by elastic forward recoil detection analysis (ERDA) using a 2 MV tandem ion accelerator. The film density was calculated from the plasmon energy using the formula for a free electron system:

$$\omega_p^2 = \frac{Ne^2}{\varepsilon_0 m},$$

where $N$ and $m$ are the electron density in electrons per unit volume and the electron mass, respectively [2]. To obtain $N$ for carbon, four electrons per atom for both $sp^2$ and $sp^3$ bonding are assumed.

Microstructural information was obtained from the Raman spectra of the samples using a visible Raman spectroscopy enabled with 514.5 nm excitation laser (Renishaw Ramanscope). The obtained spectral data were fitted by Breit–Wigner–Fano (BWF) function for the G peak and a Lorentzian function for the D peak. The BWF function contains three fitting parameters including the coupling coefficient (Q) that is a measure of the degree of symmetry of the peak [36].

X-ray photoelectron spectroscopy (XPS) analysis of HiPIMS carbon films was carried out using an Al K$\alpha$ x-ray source. The obtained spectra were fitted by two major Gaussian-Lorentzian product line shapes centred at $285.2 \pm 0.1$ eV and $284.4 \pm 0.1$ eV corresponding to $sp^3$ and $sp^2$-hybridized carbons, respectively; while a Shirley background was applied. Three other minor peaks at higher binding energies associated with carbon-oxygen bonding (C-O, C = O, O-C = O) were also included. The peak fitting was carried out using CasaXPS software.

## 3. Results

### 3.1. Electron energy loss spectrometry (EELS)

The K-edge regions for the films deposited at the target-substrate central axis and for those deposited at the extreme position (+8 cm from central axis) are shown in figures 3(a) and (b), respectively. The evaluation of the $\pi^*$ peak in the carbon K edge and the shift observed in the plasmon peak energy in the low loss region enable evaluation of the $sp^3$ content and the density of the film, respectively. The $sp^3$ fraction and the film density as a function of substrate position are shown in figures 3(c) and (d), respectively. The maximum fraction of $sp^3$ bonding in the HiPIMS film was found to be at the central axis with a value of approximately 78%. The plasmon peak is centred at 31.3 eV for the sample deposited at the central axis corresponding to a density of 3.15 g cm$^{-3}$, while the density falls to 2.87 g cm$^{-3}$ for the samples deposited 8 cm away from the central axis.

### 3.2. X-ray photoelectron spectroscopy (XPS)

XPS analysis was utilized to examine the carbon bonding states in detail and obtain another measure of the $sp^3$ fraction in the films. XPS data showed no impurities except for small concentrations of oxygen on the samples. The XPS C1s high resolution spectra for the films deposited at the central axis (positioned at 0 cm) and the extreme position (8 cm) are shown in figure 4(a). These spectra were fitted by two peaks at $285.2 \pm 0.1$ and 284.4 eV $\pm$ 0.1 corresponding to $sp^3$ and $sp^2$ bonding, respectively. Two other smaller peaks at higher binding energies were also fitted that are associated with carbon-oxygen bonds, most likely the result of surface oxidation upon exposure of samples to atmosphere. The position of C1s peak shifts to higher binding energies for the samples near to the central axis (figure 4(a)), indicating an enhancement in $sp^3$ bonding. The detailed variations of the $sp^3$ fraction calculated from peak fitting of the XPS spectra are shown as a function of distance from the central axis in figure 4(b). The $sp^3$ fractions determined from XPS lie within 4% of the values obtained

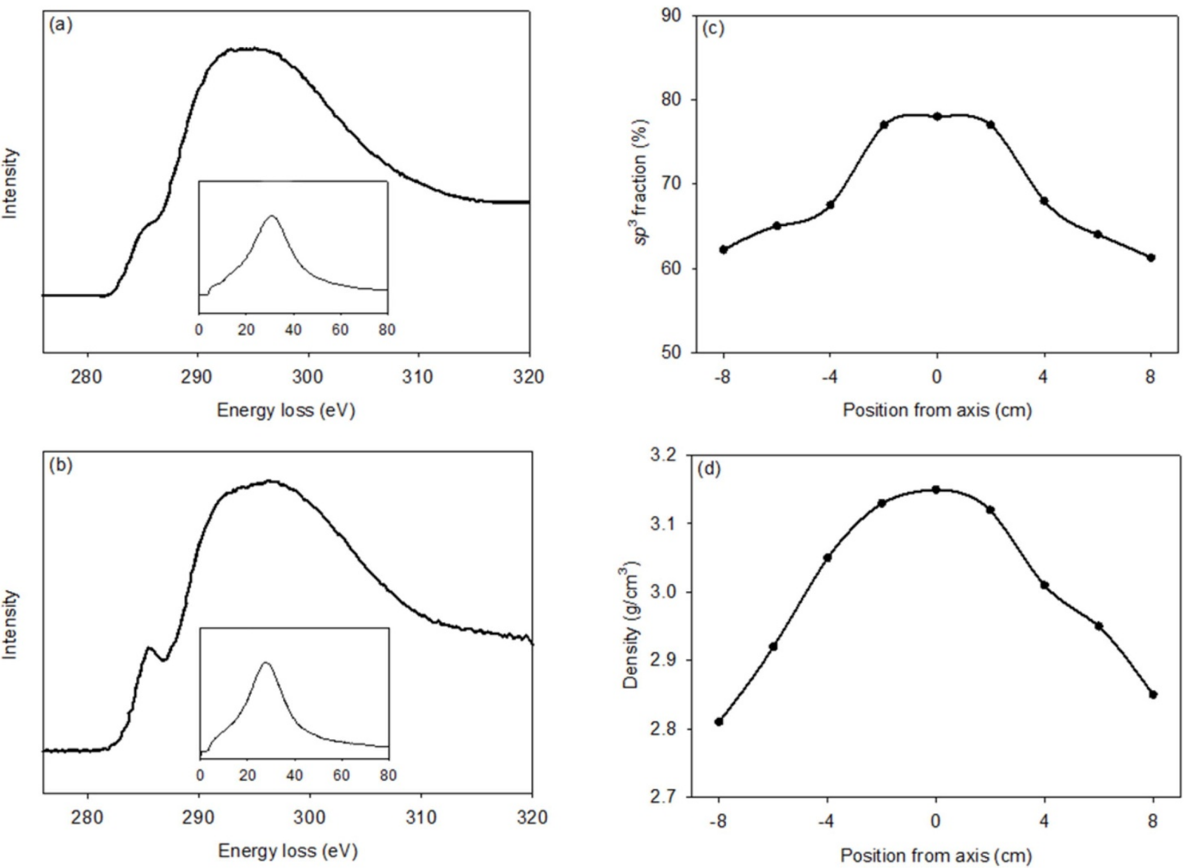


**Figure 3.** Electron energy loss spectroscopy of the carbon K edge and low loss spectra (insets) for samples deposited (a) on the central axis and (b) 8 cm from the central axis. (c) $sp^3$ fraction and (d) density as a function of distance from the central axis.

from EELS. Since EELS has been the accepted method for determining the $sp^3$ fraction [37], these results demonstrate the reliability of XPS for measuring the $sp^3$ fraction in carbon films. The depth profiles of the Ar content at various distances from the central axis, shown in figure 4(c), were obtained by XPS analysis during sputter etching using xenon. The highest argon content was obtained for the film deposited at the axial position.

### 3.3. Raman spectroscopy

The Raman spectra, shown in figure 5(a), are strongly dependent on the distance of the sample from the central axis, and their variation is consistent with the changes of $sp^3$ fraction obtained from EELS (figure 3) and XPS (figure 4) data. Similar Raman spectra were recorded for all the samples, and they consisted of only the G peak around 1580 $cm^{-1}$ with nearly no D peak around 1350 $cm^{-1}$. In figures 5(a) and (b), the peaks visible in the spectra at 960 $cm^{-1}$ are caused by the excitation of the silicon substrate by the laser light passing through the carbon film. The coupling coefficient (Q) and G-peak position of BWF fits to the Raman spectra as a function of position from the central axis are shown in figure 5(b). Lower values of Q represent higher symmetry in the carbon peak and higher $sp^3$ concentration. These data show that the Raman spectrum is more symmetric for the samples deposited at the central axis. Raman spectra for samples on the central axis show almost no D peak. As a result, the intensity ratio of the D and G peaks ($I_{(D)}/I_{(G)}$) becomes almost zero, indicating that the $sp^2$ content in the film is minimal. These films were therefore classified as ta-C. The intensity of the Si peak at 960 $cm^{-1}$ increases for the samples closer to the central axis, supporting the finding of high $sp^3$ content for these samples. The higher $sp^3$ content makes the carbon films more optically transparent [23, 38], and therefore the intensity of the Raman spectrum from the silicon substrate becomes more evident.

### 3.4. Spectroscopic ellipsometry

Figure 6 shows film deposition rate, compressive stress, refractive index ($n$), and the extinction coefficient ($k$) as a function of wavelength for the films deposited on the central axis and at a position 8 cm away from the central axis. The optical results were determined using spectroscopic ellipsometry, and the compressive stress was determined by changes in substrate curvature. The thicknesses of the carbon films, determined from the optical model used in spectroscopic ellipsometry, decrease as a function of distance from the central axis and were within 3% of the values obtained using profilometry (figure 6(a)). For the films deposited at extreme positions of 8 cm from the central axis, $n$ decreases from 2.7 to 2.2 as a function of wavelength (figure 6(b)). Higher values

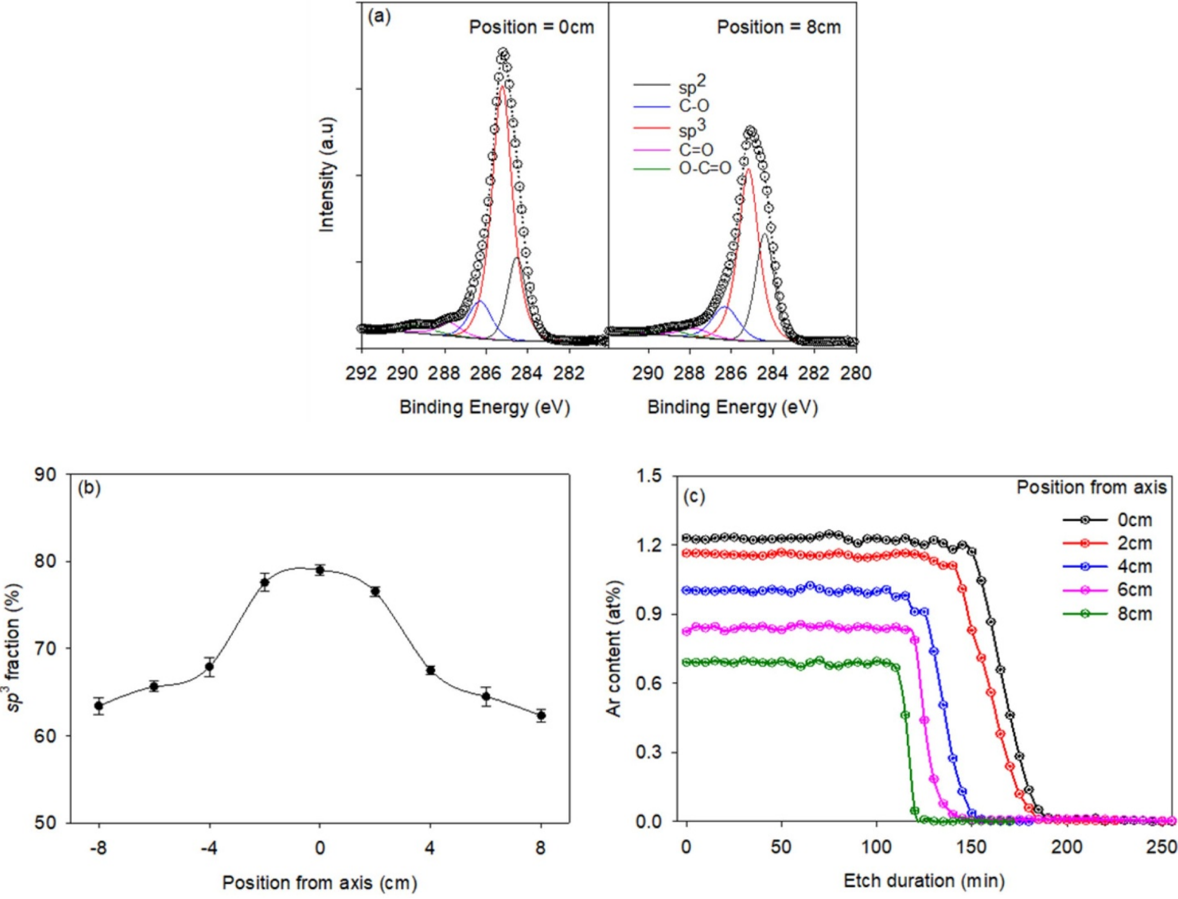


**Figure 4.** (a) XPS spectra obtained from the surfaces of the films deposited on the central axis (0 cm) and at the extreme position (8 cm). The black dots are the data points. The dotted lines passing through the data points are the sum of all fitted curves. (b) $sp^3$ fraction obtained from peak fitting of the C1s XPS high resolution spectra as a function of distance from the central axis. (c) Depth profiles of the argon concentration in the films as measured by XPS at various distances from the central axis.

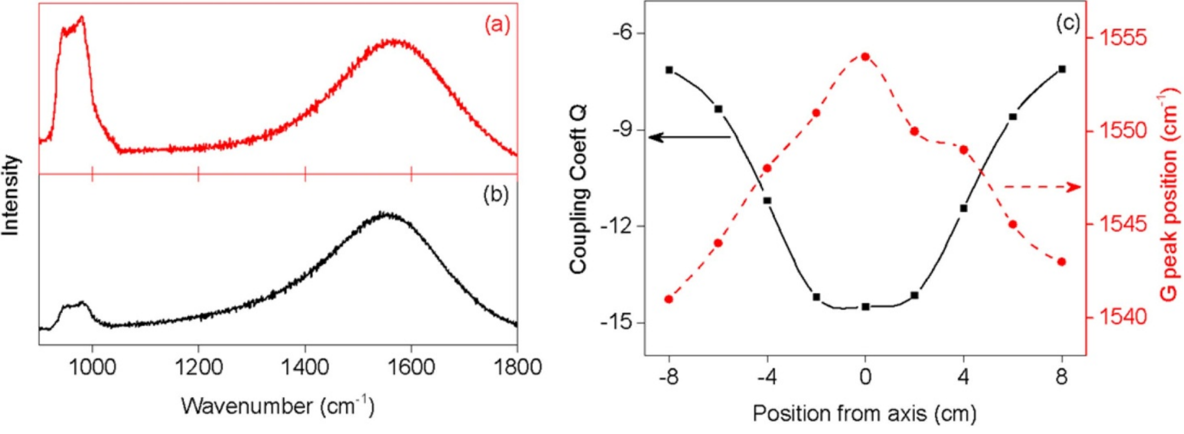


**Figure 5.** Visible Raman (514.5 nm) spectra for the films deposited on (a) the central axis and (b) 8 cm from the central axis. The peak at 960 $cm^{-1}$ arises from excitation of the silicon substrate. (c) Coupling coefficient (Q) and G-peak position of BWF fits to the spectra as a function of position from the central axis. Lower values of Q represent higher symmetry in the carbon peak and higher $sp^3$ concentration.

of $k$ in the visible region were obtained for the films deposited at the extreme positions, indicating a higher absorption in those films. Figure 6(d) shows the determination of optical band gaps of the carbon films by extrapolating the linear fit applied around the inflection point of plots of $(\alpha h\nu)^{1/2}$ versus $E(h\nu)$, where '$h\nu$' and '$\alpha$' are the photon energy and the absorption coefficient, respectively. The optical bandgaps as a function of the distance away from the central axis are

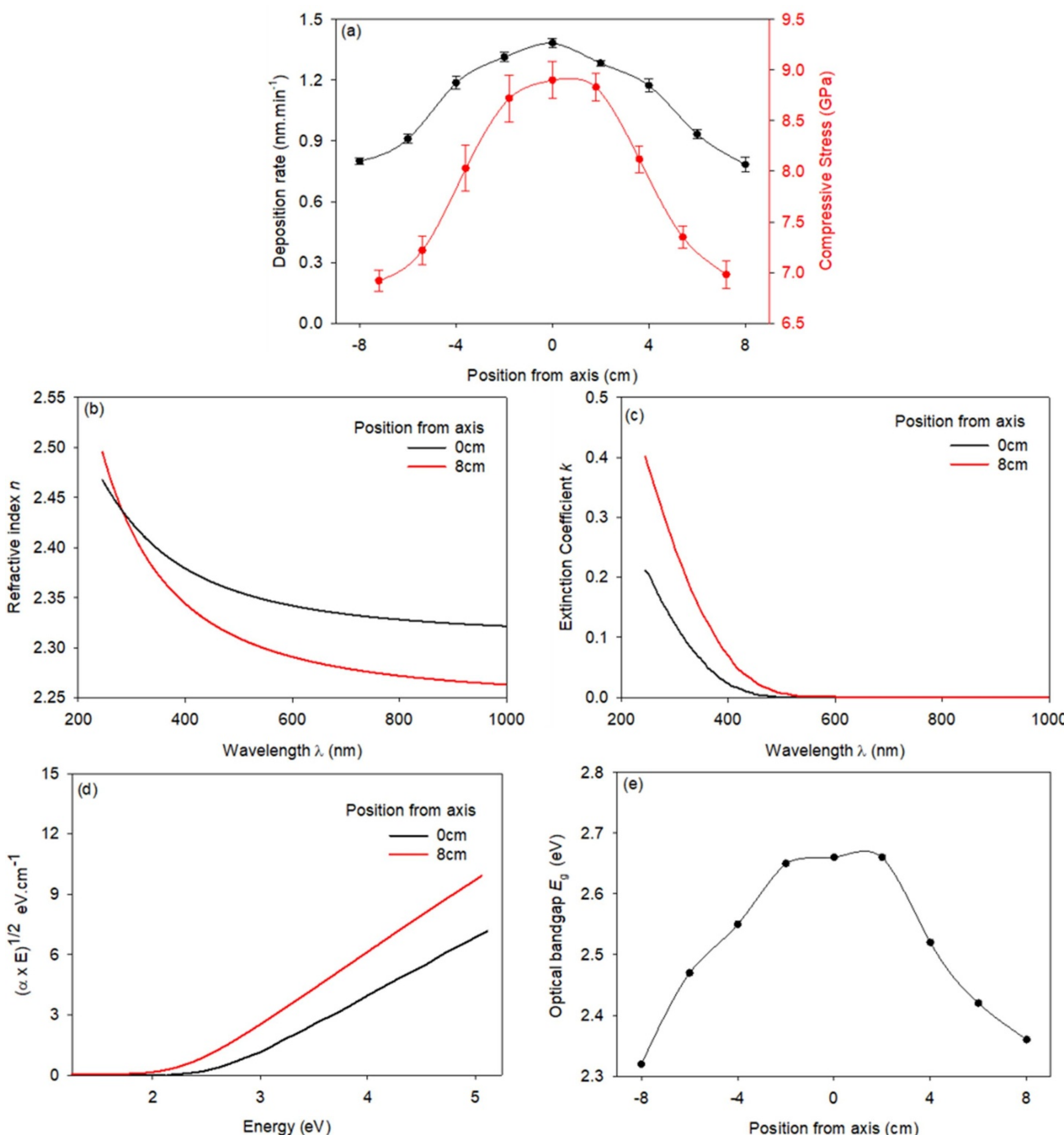


**Figure 6.** (a) Deposition rate and compressive stress for the films deposited at various distances from the central axis with an external magnetic field applied by the solenoidal coil. The deposition rate for the films placed on the central axis exhibited the highest enhancement (2.76 times in comparison with the HiPIMS without the presence of external magnetic field) as a result of the application of the magnetic field. The wavelength dispersion of (b) $n$ and (c) $k$ for the films deposited at the positions of 0 and 8 cm from the central axis. The corresponding Tauc plots are presented in (d) and determine the optical bandgap. (e) Optical bandgaps of films deposited as a function of position from the central axis.

plotted in figure 6(e). The optical bandgap reduces for films deposited with increasing distance from the axis, indicative of increasing $sp^2$ content in agreement with the results of EELS (figure 3), XPS (figure 4), and Raman spectroscopy (figure 5).

### *3.5. Electrical characterization*

Current-voltage characteristics from the metal-insulator-semiconductor devices are shown in figure 7. These characteristics are nonlinear and depend strongly on the position of each device relative to the central axis at 0 cm during carbon deposition. The I–V characteristic measured from a device located at 0 cm exhibits measurable hysteresis. Both hysteresis (measured by the area enclosed) and a region of negative differential resistance (NDR, measured by the range over which dI/dV is negative) become increasingly pronounced in devices made with films deposited at greater distances from the axis (0 cm). The occurrence of hysteresis and negative differential resistance are therefore correlated with the $sp^2$

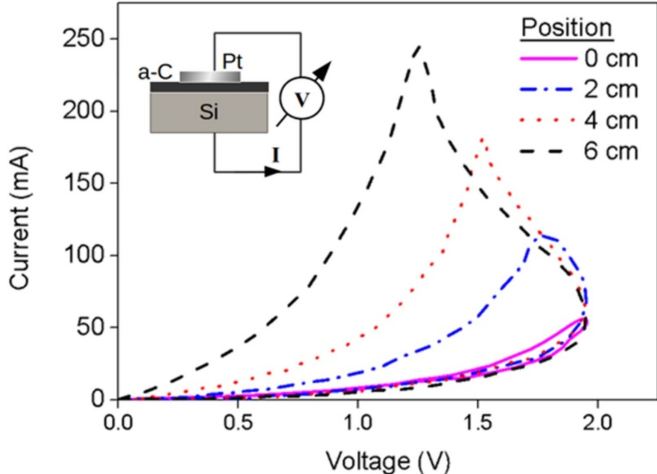


**Figure 7.** Nonlinear I–V characteristics from Metal-insulator-semiconductor (MIS) devices formed on the a-C films at various distances from the central axis. The inset shows the MIS device structure. Hysteresis and negative differential resistance are evident.

content of the films which increases with distance from the central axis.

### *3.6. Ion current measurements at the substrate*

The peak ion current during a pulse, integrated over a disk of 1 cm diameter as a function of position on the substrate holder with and without the magnetic field produced by the coil is shown in figure 8. The ion current is uniform in the absence of the magnetic field (figure 8(a)), while it increases with proximity to the target-substrate axis in the presence of the field (figure 8(b)). The ion energy distribution measured using the retarding field energy analyser (RFEA) on the central axis in the absence and presence of the magnetic field is shown in figures 8(c) and (d), respectively. Figure 8(e) shows the magnetic field direction and strength on a vertical slice passing through the centre of the coil, simulated using COMSOL.

The magnetic field causes significant changes in the plasma parameters in the vicinity of the substrate by focusing the ions towards the substrate and enhancing ion flux at the positions closer to the central axis (figures 8(a) and (b)).

## 4. Discussion

We have demonstrated the use of a magnetic field created by a solenoid coil to increase the $sp^3$ fraction of carbon films deposited using mixed mode HiPIMS. The acceleration of ions in a diverging magnetic field produced high $sp^3$ fraction films in the range of ta-C, with only a small substrate bias, typical of that acquired by an electrically floating substrate. The ion accelerating effect of the diverging magnetic field we have observed (figures 8(c) and (d)) is likely to be due to the end-Hall effect [39]. The kinetic energy from this acceleration is added to the energy obtained from the electrostatic acceleration due to the negative floating potential of an insulating substrate. The energy from these two sources enables the deposition of ta-C onto insulators, which is of value in the production of ta-C films for wear protection or encapsulation [40].

The $sp^3$ fraction of the deposited films was determined using EELS (figure 3) and XPS (figure 4) and was observed to be a maximum on the axis of the magnetic coil. The Raman signal (figure 5), optical properties (figure 6) and electrical conductivity (figure 7) are consistent with the maximal $sp^3$ content on axis, decreasing with distance from the axis.

The increasing dispersion in the refractive index and extinction coefficient and the decreasing optical bandgap in the films as a function of position away from central axis (figures 6(b)–(e)) can be attributed to the decreasing trend in the deposition rate (figures 6(a) and 8(b)) and energy of ions, a critical parameter that controls $sp^3$ content (figures 3(c), 4(b), and 5). This is in accordance with theoretical [24, 41] and experimental observations [21, 23, 25] that there is an optimum ion energy range for ta-C film formation, which provides appropriate compressive stress to promote $sp^3$ bonding.

Our results also show that the $sp^3$ content is linked to the energy of the depositing flux as confirmed by its dependence on location. The fact that ion energy decreases from the centre to the edge is demonstrated by the same location dependence of the depth of Ar ion implantation (figure 4(c)). The argon atomic concentration is also maximized on axis, indicative of the ion focusing effect of the coil which increases the deposition rate at the substrate centre relative to its edge (figures 4(c) and 6(a)). This ion-focusing effect is also directly observed through spatially resolved ion current measurements in the plasma (figures 8(a) and (b)). The enhancement in ion flux at the centre of the magnetic field produced by the coil is a result of an ambipolar electric field that traps ions inside a potential well [42]. This potential well is created by magnetised electrons that are restricted to move along the field lines by virtue of their motion in orbits that gyrate around the field lines [43]. This focusing effect is also responsible for the increase in deposition rate observed (figure 6(a))

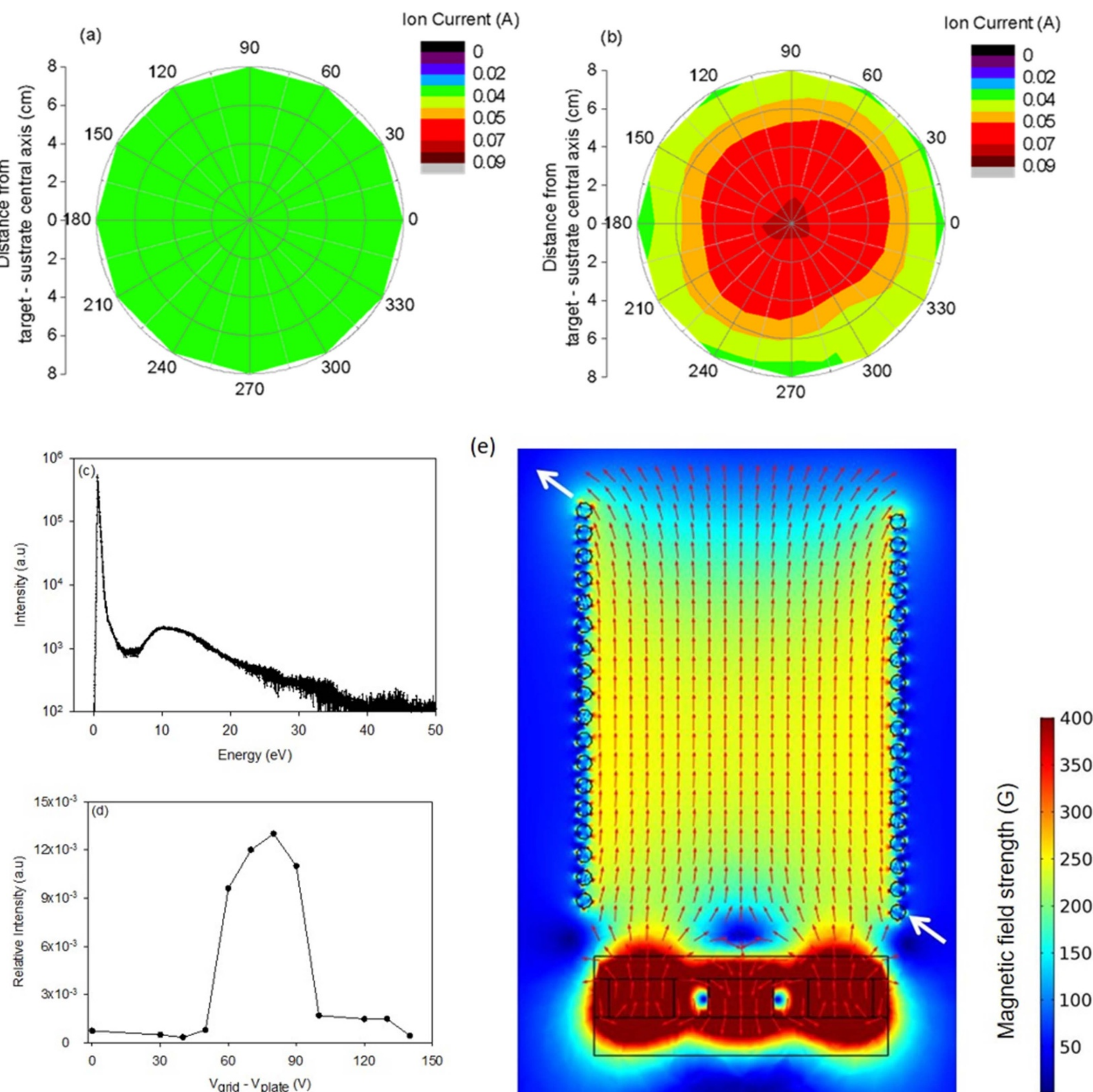


**Figure 8.** The peak current received by the retarding field energy analyser (RFEA), plotted using linear interpolation between measurements, at various locations at the substrate (a) without and (b) in the presence of magnetic field produced by current in the coil. Magnetic field increases the ion fluence by transporting plasma to the substrate region and focuses the plasma at the centre. (c) Ion energy distribution measured using the RFEA on the central axis in the absence of a coil. (d) Ion energy distribution measured using an RFEA on the central axis in the presence of the coil carrying a current of 120 A. (e) The magnetic field strength simulated using COMSOL plotted on a slice through the centre of the coil. The arrows indicate the direction of field and the intensity is indicated by the colour scale.

as it redirects much of the sideways flux noted in previous work [44] towards the substrate. The focusing effect of the magnetic coil has another benefit in reducing the macroparticle content of the films deposited near the central axis, arising from the increase of the flux of ions relative to the flux of macroparticles. A reduced content of macroparticles is especially important in the optical and electronic applications of ta-C.

In this work, we observe a correlation between the atomic percentage Ar content and deposition rate (figures 4(c) and 6(a)). This is likely due to the fact that trapping probability of argon increases with increasing incident carbon flux [45]. We also observe a correlation between Ar content and stress (figures 4(c) and 6(a)). Although correlations between the argon content and the compressive stress have previously been reported [46–48], they do not appear

to be causal, as other works observed no correlation [49, 50] or correlation only when the pressure is low enough that energy is not dissipated by collisions on route to the substrate [21].

The through-film current voltage (I–V) characteristics of the films showed non-linear and hysteretic behaviour which increased systematically with substrate position relative to the central axis of the magnetic coil during carbon deposition, leading in some cases to negative differential resistance (NDR). The conductance (dI/dV) extracted at 1.0 V from the low resistance paths in these I–V characteristics increases with the distance from 0 cm and hence with the $sp^2$ fraction. Similar characteristics have been observed previously in memristor devices with oxygenated amorphous carbon layers [51]. In that work, the addition of oxygen during sputter deposition was suggested as the cause of the effect. However, it has been shown recently that the oxygen content is not necessary for the appearance of resistive switching in amorphous carbon and that it appears to be associated with the optimal content of $sp^2$ carbon atoms [52]. Furthermore, it is possible to fabricate memristors entirely from carbon with layers of high $sp^2$ content carbon acting as ohmic contacts to the memristive layer of intermediate $sp^2$ content [53]. We attribute the memristive behaviour in our devices to a mechanism associated with changes in the bonding of the $sp^2$ carbon atoms [54]. The ability to produce carbon films with controllable $sp^2$ content as shown in this work is of interest in tuning the performance of memristor devices/arrays.

HiPIMS systems integrated with an external magnetic field to guide ion deposition are attractive for use in large-scale manufacturing. The deposition of HiPIMS coatings on large area surfaces with high throughput could be achieved in industrial coating machines using either a large rectangular cathode with a rectangular cross section coil or an array of multiple smaller circular cathodes fitted with individual magnetic coils. Linear or annular slits could be used to select the appropriate $sp^3$ fraction in the rectangular or circular cathodes, respectively. Uniformity of the coating could be achieved by scanning the substrate relative to the selected depositing flux.

## 5. Conclusions

Using the magnetic field-assisted HiPIMS sputtering technique presented in this paper, it is possible to deposit ta-C films by sputtering with controlled $sp^3$ fraction onto insulating substrates, without the need for electrical bias to be applied. The magnetic field focuses the plasma, resulting in an increase of $sp^3$ fraction, density, and compressive stress towards the axis of the magnetic field coil. This increase in $sp^3$ fraction is due to an increase in ion energy with decreasing distance from the axis of the magnetic field coil. A further benefit is that the deposition rate on the axis of the magnetic coil is significantly higher than that achievable without the presence of external magnetic field. The films produced using the magnetic field-assisted HiPIMS process show tuneable memristive switching behaviour which increases with decreasing $sp^3$ content. These films are of great interest for a wide variety of applications including resistive switching devices for neuromorphic technologies.

## ORCID iDs

Behnam Akhavan https://orcid.org/0000-0002-1599-658X
David R McKenzie https://orcid.org/0000-0002-2476-1301
Marcela MM Bilek https://orcid.org/0000-0003-3363-2664

## References

[1] McKenzie D, Yin Y, Marks N, Davis C, Kravtchinskaia E, Pailthorpe B and Amaratunga G 1993 Tetrahedral amorphous carbon properties and applications *J. Non-Cryst. Solids* **164** 1101–6
[2] McKenzie D 1996 Tetrahedral bonding in amorphous carbon *Rep. Prog. Phys.* **59** 1611
[3] Robertson J 2002 Diamond-like amorphous carbon *Mater. Sci. Eng.* R **37** 129–281
[4] Wei J, Guo P, Liu L, Li H, Li H, Wang S, Ke P, Saito H and Wang A 2020 Corrosion resistance of amorphous carbon film in 3.5 wt% NaCl solution for marine application *Electrochim. Acta* **346** 136282
[5] Wu J, Wu G, Kou X, Lu Z and Zhang G 2019 Tribological properties of amorphous carbon in hydrochloric acid with ta-C counterpart *Surf. Coat. Technol.* **380** 125004
[6] Palomäki T, Peltola E, Sainio S, Wester N, Pitkänen O, Kordas K, Koskinen J and Laurila T 2018 Unmodified and multi-walled carbon nanotube modified tetrahedral amorphous carbon (ta-C) films as in vivo sensor materials for sensitive and selective detection of dopamine *Biosens. Bioelectron.* **118** 23–30
[7] Cho Y-S, Liao L-K, Hsu C-H, Hsu Y-H, Wu W-Y, Liao S-C, Chen K-H, Lui P-W, Zhang S and Lien S-Y 2019 Effect of substrate bias on biocompatibility of amorphous carbon coatings deposited on Ti6Al4V by PECVD *Surf. Coat. Technol.* **357** 212–7
[8] Romero P A, Pastewka L, Von Lautz J and Moseler M 2014 Surface passivation and boundary lubrication of self-mated tetrahedral amorphous carbon asperities under extreme tribological conditions *Friction* **2** 193–208
[9] Götze A, Makowski S, Kunze T, Hübner M, Zellbeck H, Weihnacht V, Leson A, Beyer E, Joswig J O and Seifert G 2014 Tetrahedral amorphous carbon coatings for friction reduction of the valve train in internal combustion engines *Adv. Eng. Mater.* **16** 1226–33
[10] Lappalainen R, Selenius M, Anttila A, Konttinen Y T and Santavirta S S 2003 Reduction of wear in total hip replacement prostheses by amorphous diamond coatings *J. Biomed. Mater. Res.* B **66** 410–3
[11] Grill A 2003 Diamond-like carbon coatings as biocompatible materials—an overview *Diamond Relat. Mater.* **12** 166–70
[12] Decker T G, Lundy G P, Pappas D L, Welty R P and Parent C R 1999 Amorphous diamond coating of blades Google Patents
[13] Palomäki T, Wester N, Caro M A, Sainio S, Protopopova V, Koskinen J and Laurila T 2017 Electron transport determines the electrochemical properties of tetrahedral amorphous carbon (ta-C) thin films *Electrochim. Acta* **225** 1–10
[14] Martin P, Filipczuk S, Netterfield R, Field J, Whitnall D and McKenzie D 1988 Structure and hardness of diamond-like carbon films prepared by arc evaporation *J. Mater. Sci. Lett.* **7** 410–2

[15] Fallon P, Veerasamy V, Davis C, Robertson J, Amaratunga G, Milne W and Koskinen J 1993 Properties of filtered-ion-beam-deposited diamondlike carbon as a function of ion energy *Phys. Rev.* B **48** 4777
[16] Voevodin A and Donley M 1996 Preparation of amorphous diamond-like carbon by pulsed laser deposition: a critical review *Surf. Coat. Technol.* **82** 199–213
[17] Kulik J, Lifshitz Y, Lempert G, Rabalais J and Marton D 1994 Electron-energy-loss spectroscopy of mass-selected ion-beam-deposited diamondlike carbon *J. Appl. Phys.* **76** 5063–9
[18] Kulik J, Lempert G, Grossman E, Marton D, Rabalais J and Lifshitz Y 1995 s p 3 content of mass-selected ion-beam-deposited carbon films determined by inelastic and elastic electron scattering *Phys. Rev.* B **52** 15812
[19] Anders A 2010 Unfiltered and filtered cathodic arc deposition *Handbook of Deposition Technologies for Films and Coatings* (Amsterdam: Elsevier) pp 466–531
[20] Bewilogua K and Hofmann D 2014 History of diamond-like carbon films—from first experiments to worldwide applications *Surf. Coat. Technol.* **242** 214–25
[21] Ganesan R, McCulloch D, Marks N, Tucker M, Partridge J, Bilek M and McKenzie D 2015 Synthesis of highly tetrahedral amorphous carbon by mixed-mode HiPIMS sputtering *J. Phys. D: Appl. Phys.* **48** 442001
[22] Ganesan R, Akhavan B, Hiob M A, McKenzie D R, Weiss A S and Bilek M M M 2018 HiPIMS carbon coatings show covalent protein binding that imparts enhanced hemocompatibility *Carbon* **139** 118–28
[23] Tucker M, Ganesan R, McCulloch D, Partridge J, Stueber M, Ulrich S, Bilek M, McKenzie D and Marks N 2016 Mixed-mode high-power impulse magnetron sputter deposition of tetrahedral amorphous carbon with pulse-length control of ionization *J. Appl. Phys.* **119** 155303
[24] Robertson J 2005 Mechanism of sp3 bond formation in the growth of diamond-like carbon *Diamond Relat. Mater.* **14** 942–8
[25] Schwan J, Ulrich S, Roth H, Ehrhardt H, Silva S, Robertson J, Samlenski R and Brenn R 1996 Tetrahedral amorphous carbon films prepared by magnetron sputtering and dc ion plating *J. Appl. Phys.* **79** 1416–22
[26] Schwan J, Ulrich S, Theel T, Roth H, Ehrhardt H, Becker P and Silva S 1997 Stress-induced formation of high-density amorphous carbon thin films *J. Appl. Phys.* **82** 6024–30
[27] Ganesan R, Akhavan B, Partridge J G, McCulloch D G, McKenzie D R and Bilek M M 2017 Evolution of target condition in reactive HiPIMS as a function of duty cycle: an opportunity for refractive index grading *J. Appl. Phys.* **121** 171909
[28] Najafi-Ashtiani H, Akhavan B, Jing F and Bilek M M 2019 Transparent conductive dielectric− metal− dielectric structures for electrochromic applications fabricated by high-power impulse magnetron sputtering *ACS Appl. Mater. Interfaces* **11** 14871–81
[29] Ganesan R, Treverrow B, Denniss P, McCulloch D G, McKenzie D R and Bilek M M M 2016 Pulsed external magnetic fields increase the deposition rate in reactive HiPIMS while preserving stoichiometry: an application to amorphous $HfO_2$ *J. Appl. Phys.* **120** 103301
[30] Ganesan R, Akhavan B, Dong X, McKenzie D R and Bilek M M M 2018 External magnetic field increases both plasma generation and deposition rate in HiPIMS *Surf. Coat. Technol.* **352** 671–9
[31] Bathgate S N, Ganesan R, Bilek M M and McKenzie D R 2016 A HiPIMS plasma source with a magnetic nozzle that accelerates ions: application in a thruster *Eur. Phys. J. Appl. Phys.* **76** 30801
[32] Bathgate S N, Bilek M M, Cairns I H and McKenzie D R 2018 A thruster using magnetic reconnection to create a high-speed plasma jet *Eur. Phys. J. Appl. Phys.* **84** 20801
[33] Bathgate S, Bilek M and Mckenzie D 2017 Electrodeless plasma thrusters for spacecraft: a review *Plasma Sci. Technol.* **19** 083001
[34] Herzinger C, Johs B, McGahan W, Woollam J A and Paulson W 1998 Ellipsometric determination of optical constants for silicon and thermally grown silicon dioxide via a multi-sample, multi-wavelength, multi-angle investigation *J. Appl. Phys.* **83** 3323–36
[35] Berger S, McKenzie D and Martin P 1988 EELS analysis of vacuum arc-deposited diamond-like films *Phil. Mag. Lett.* **57** 285–90
[36] Prawer S, Nugent K, Lifshitz Y, Lempert G, Grossman E, Kulik J, Avigal I and Kalish R 1996 Systematic variation of the Raman spectra of DLC films as a function of sp2: sp3 composition *Diamond Relat. Mater.* **5** 433–8
[37] Papworth A, Kiely C, Burden A, Silva S and Amaratunga G 2000 Electron-energy-loss spectroscopy characterization of the sp 2 bonding fraction within carbon thin films *Phys. Rev.* B **62** 12628
[38] Chhowalla M, Ferrari A, Robertson J and Amaratunga G 2000 Evolution of sp 2 bonding with deposition temperature in tetrahedral amorphous carbon studied by Raman spectroscopy *Appl. Phys. Lett.* **76** 1419–21
[39] Kaufman H R, Robinson R S and Seddon R I 1987 End-Hall ion source *J. Vac. Sci. Technol.* A **5** 2081–4
[40] Amanat N, Nicoll A F, Ruys A J, McKenzie D R and James N L 2011 Gas permeability reduction in PEEK film: comparison of tetrahedral amorphous carbon and titanium nanofilm coatings *J. Membr. Sci.* **378** 265–71
[41] McKenzie D, Muller D and Pailthorpe B 1991 Compressive-stress-induced formation of thin-film tetrahedral amorphous carbon *Phys. Rev. Lett.* **67** 773
[42] Bilek M, Yin Y and McKenzie D 1996 A study of filter transport mechanisms in filtered cathodic vacuum arcs *IEEE Trans. Plasma Sci.* **24** 1165–73
[43] Bilek M 1999 The effect of magnetic field configuration on plasma beam profiles in curved magnetic filters *J. Appl. Phys.* **85** 6385–91
[44] Hajihoseini H, Čada M, Hubička Z, Ünaldi S, Raadu M A, Brenning N, Gudmundsson J T and Lundin D 2020 Sideways deposition rate and ionized flux fraction in dc and high power impulse magnetron sputtering *J. Vac. Sci. Technol.* A **38** 033009
[45] Paturaud C, Farges G, Sainte Catherine M and Machet J 1999 Correlation between hardness and embedded argon content of magnetron sputtered chromium films *Thin Solid Films* **347** 46–55
[46] Nissim A, Raveh A, Sariel J and Mintz M 2007 Effect of substrate bias voltage on the properties of magnetron-sputtered gadolinium layers *Surf. Coat. Technol.* **201** 7054–9
[47] Klett A, Freudenstein R and Kulisch W 2001 Dependence of the stress of c-BN films on the major deposition parameters: theoretical and experimental studies *Thin Solid Films* **398** 130–6
[48] Akhavan B, Ganesan R, Stueber M, Ulrich S, McKenzie D R and Bilek M M M 2019 Carbon films deposited by mixed-mode high power impulse magnetron sputtering for high wear resistance: the role of argon incorporation *Thin Solid Films* **688** 137353
[49] Thornton J A, Tabock J and Hoffman D 1979 Internal stresses in metallic films deposited by cylindrical magnetron sputtering *Thin Solid Films* **64** 111–9
[50] Hoffman D and Thornton J A 1979 Effects of substrate orientation and rotation on internal stresses in sputtered metal films *J. Vac. Sci. Technol.* **16** 134–7
[51] Santini C A, Sebastian A, Marchiori C, Jonnalagadda V P, Dellmann L, Koelmans W W, Rossell M D, Rossel C P

and Eleftheriou E 2015 Oxygenated amorphous carbon for resistive memory applications *Nat. Commun.* **6** 1–9

[52] Murdoch B, Raeber T, Zhao Z, McKenzie D, McCulloch D and Partridge J 2019 Temperature sensitivity and short-term memory in electroforming-free low power carbon memristors *Appl. Phys. Lett.* **114** 163504

[53] Raeber T J, Zhao Z C, Murdoch B J, McKenzie D R, McCulloch D G and Partridge J G 2018 Resistive switching and transport characteristics of an all-carbon memristor *Carbon* **136** 280–5

[54] Raeber T, Barlow A, Zhao Z, McKenzie D, Partridge J, McCulloch D and Murdoch B 2018 Sensory gating in bilayer amorphous carbon memristors *Nanoscale* **10** 20272–8